mater.scichina.com link.springer.com

Published online 8 June 2022 | https://doi.org/10.1007/s40843-021-2049-9
Sci China Mater 2022, 65(9): 2335–2342

Unshackling the reversible capacity of SiO_x/graphite-based full cells *via* selective LiF-induced lithiation

Jinran Sun[1,2†], Shu Zhang[1†], Qinghua Zhang[3], Yunchuan Xin[1], Shamu Dong[1*], Haisheng Liu[1], Jiedong Li[1], Chao Wang[1], Chenglong Lu[1], Wuhai Yang[1], Tingting Liu[1,2], Jun Ma[1], Lin Gu[3] and Guanglei Cui[1,2*]

ABSTRACT **Composite Si@SiO_x/C anodes with high specific capacity are considered the most promising alternatives to graphite in industrial lithium-ion batteries. However, their cycling stability remains a limiting factor, which originates from the severe volume deformation of silicon-derived species. In this work, the cyclabilities of composite anodes are improved by unshackling the highly reversible lithium storage capabilities from the redundancy capacity of the anode materials. A selective LiF-induced lithiation strategy is proposed based on exploiting interface separation energy differences between LiF and the active materials. An interesting preferential redeposition of LiF is observed at the Si@SiO_x particles, which differentiates the otherwise similar lithiation potentials of LiC_x and $Li_{15}Si_4$, thereby enabling lithium storage in graphite that was previously underused. The resulting full cell exhibits better rate and cycling performances without sacrificing specific capacity. In an ultra-high area capacity full cell (4.9 mA h cm^{-2}), the capacity retention increases markedly from 66.1% to 94.2% after 300 cycles. The selective lithiation strategy developed herein is feasible for practical industrial applications, and importantly, it requires no changes to the existing mature lithium-ion battery manufacturing process. This study offers a new approach for the development of silicon/graphite composite anodes with long cycling lifetimes.**

Keywords: silicon-based composite anode, cyclability, selective lithiation, LiF, interface separation energy

INTRODUCTION

Continuous updates to new-energy electric vehicles require Li-ion batteries (LIBs) with higher energy density; therefore, it is crucial to develop electrode materials with high specific capacity to satisfy the ever-growing energy density requirements. Recently, Si-based composite anodes have attracted significant interest as promising candidates for next-generation anodes because of their relatively high specific capacity [1–5].

Two issues limit the practical application of Si-based composite materials: low initial columbic efficiency (ICE) and poor cycling performance [6,7]. The low ICE is primarily caused by the formation of the initial solid-electrolyte-interphase (SEI) [8,9]. Because the cathode is the only lithium source in a full cell, the loss of active lithium at the SEI reduces the reversible capacity, thereby degrading the energy density [10–16]. It is well established that this issue can be mitigated by applying a pre-lithiation technique. Chemical pre-lithiation is commonly employed in industrial applications owing to its high compatibility with the existing production process. Various reagents that are rich in lithium have been used for chemical pre-lithiation, including Li_3N, Li_3P, Li_2S, Li_2O, and Li_2O_2 [17–20]. To compensate for the active lithium losses, the pre-lithiation reagents donate extra lithium through irreversible decomposition. Direct contact between the anode and the lithium foil (e.g., during rolling or evaporation deposition) can also effectively improve the ICE by introducing an additional lithium source to the active materials prior to battery operation [21–23]. Although improving the ICE is difficult, it is even more challenging to enhance the cycling stability of Si-based composite anodes because of the drastic changes in the volume of silicon-derived species (~300%) during lithiation/delithiation [24,25]. Volume deformation during cycling can reduce the electrical contact and induce repeated fractures in the SEI; the freshly exposed surface that is generated can then trigger irreversible parasitic reactions. As a result, the continuous consumption of active lithium contributes to the poor cycling stability of Si-based composite anodes. This issue becomes more serious when the Si-based composite anode has high mass loading (to achieve industrial-level area capacity >4 mA h cm^{-2}).

Recently, scholars have explored various approaches for improving the cycling stability of Si-based composite anodes, e.g., designing Si nanostructures, applying thin layer coatings on Si, or using different binders [26–38]. Nonetheless, these methods are not appropriate for practical LIBs owing to their complexity or ultralow loading levels. It is a serious challenge to improve the cycling stability of Si-based composite anodes with high mass loading. Controlling the depth of the charge/discharge voltage is a feasible way to improve the cycling stability; however, it may require sacrificing the specific capacity of the electrode. Furthermore, it is not suitable for the widely studied Si-graphite composite systems because the formation potential of LiC_x (the lithiated product of graphite; ~100 mV) is close to that of $Li_{15}Si_4$ (the deeply lithiated product of silicon; ~100 mV)

[1] Qingdao Industrial Energy Storage Research Institute, Qingdao Institute of Bioenergy and Bioprocess Technology, Chinese Academy of Sciences, Qingdao 266101, China
[2] Center of Materials Science and Optoelectronics Engineering, University of Chinese Academy of Sciences, Beijing 100049, China
[3] Beijing National Laboratory for Condensed Matter Physics, Institute of Physics, Chinese Academy of Sciences, Beijing 100190, China
[†] These authors contributed equally to this work.
[*] Corresponding authors (emails: dongsm@qibebt.ac.cn (Dong S); cuigl@qibebt.ac.cn (Cui G))

[39,40]. In a full cell, these similar lithiation potentials also manifest in the incomplete use of graphite, because a certain redundancy capacity in the anode is necessary for preventing lithium plating [39]. An optimal value of N/P ratio (negative/positive capacity ratio) falls in the range of 1.1–1.2, which means that at least ~10% of the anode capacity is underused [41]. Unshackling the highly reversible capacity of graphite, which occupies a considerable part of that underused redundancy capacity, could markedly improve the cyclability of Si-graphite composite systems.

Herein, we propose a selective LiF-induced lithiation strategy to access the highly reversible lithium storage capabilities from the redundancy capacity of Si-based anodes. We report an improvement in the cycling stability of a pre-lithiated high-loading Si@SiO_x/C ($0 < x \leq 2$) composite anode (named as S450, with a nominal specific capacity of 450 mA h g^{-1}). Considering the interface separation energy [42] and differences between LiF and the active materials, we control the SEI on local Si@SiO_x particles with enriched LiF coverage by implementing a rationally designed dissolution and redeposition process. The preferential accumulation of LiF decelerates the lithiation kinetics at Si@SiO_x particles and allows the $Li_{15}Si_4$ to form at a lower potential. Consequently, more lithium can be stored by the graphite which has highly reversible lithium storage capability (Scheme 1). The relatively complete use of graphite increases the reversibility of the anode without sacrificing its overall capacity. In a high-area-capacity full cell (NCA($LiNi_{0.8}Co_{0.15}Al_{0.05}O_2$)/S450, 4.9 mA h cm^{-2}), the capacity retention increases markedly from 66.1% to 94.2% after 300 cycles.

EXPERIMENTAL SECTION

Electrode preparation and electrochemical measurements

The NCA cathode (active mass loading ~26 mg cm^{-2}; mass ratio = 94%) and S450 composite anode (active mass loading ~12.1 mg cm^{-2}; nominal specific capacity = 450 mA h g^{-1}) were supplied by BTR New Energy Material Ltd., China. The electrolyte comprised 1 mol L^{-1} $LiPF_6$ in diethyl carbonate (DEC, Shanghai Macklin Biochemical Co., Ltd)/fluoroethylene carbonate (FEC, Shanghai Macklin Biochemical Co., Ltd) (4:1 *v*/*v*), which was prepared according to a previous report [43]. The batteries were assembled with a polyethylene film (Celgard) separator. The N/P value of the full cell in this study was 1.09. Pre-lithiation was performed using a vacuum thermal evaporation deposition (VTED) technique (Scheme S1), and the thickness of the lithium metal could be precisely controlled using a film thickness monitor. The density of the deposited lithium metal was 0.41 g cm^{-3}; therefore, 6.25 μm of deposited lithium corresponded to an area capacity of 1 mA h cm^{-2} (the relevant calculations are detailed in the Supplementary information). LiF was deposited (thickness of ~40 nm) on the pre-lithiated anode *via* radio frequency magnetron sputtering (30 min, Beijing Jinshengweina Technology Co., Ltd) on the electrode (Scheme S1). The LiF target (50 mm diameter) from Zhongnuo Advance Material Technology Co., Ltd. (Beijing) was mounted, and the base pressure in the chamber was (1–5) × 10^{-6} mbar (1 bar = 10^5 Pa). During Ar sputtering, the pressure was 8.5 × 10^{-3} mbar, and the sputtering power was 60 W. Electrochemical tests were performed using a coin-type cell (LIR 2032), which was fabricated in a glove box filled with argon. Electrochemical performance was evaluated using a battery test system (LAND CT2001A). The batteries were cycled at a charge rate of 0.2 C and a discharge rate of 0.4 C over the voltage range of 2.8–4.2 V. All electrochemical experiments were conducted at 30°C. The reassembled batteries comprised lithium metal (Ø 15 × 0.6 mm) and the S450 anode (in the discharged state), and these batteries were charged with a cutoff voltage of 1.5 V.

Characterization

The sample morphologies were examined using field emission scanning electron microscopy (FESEM; Hitachi S-4800) combined with energy dispersive X-ray spectroscopy (EDX) to determine the elemental composition. Transmission electron microscopy (TEM) and elemental mapping were performed using high-resolution TEM (HRTEM; JEOL JEM-F200) combined with EDX to assess the elemental composition. *Ex situ* ^{7}Li and ^{6}Li nuclear magnetic resonance (NMR) spectra were recorded on a Bruker AVWB III 600 spectrometer equipped

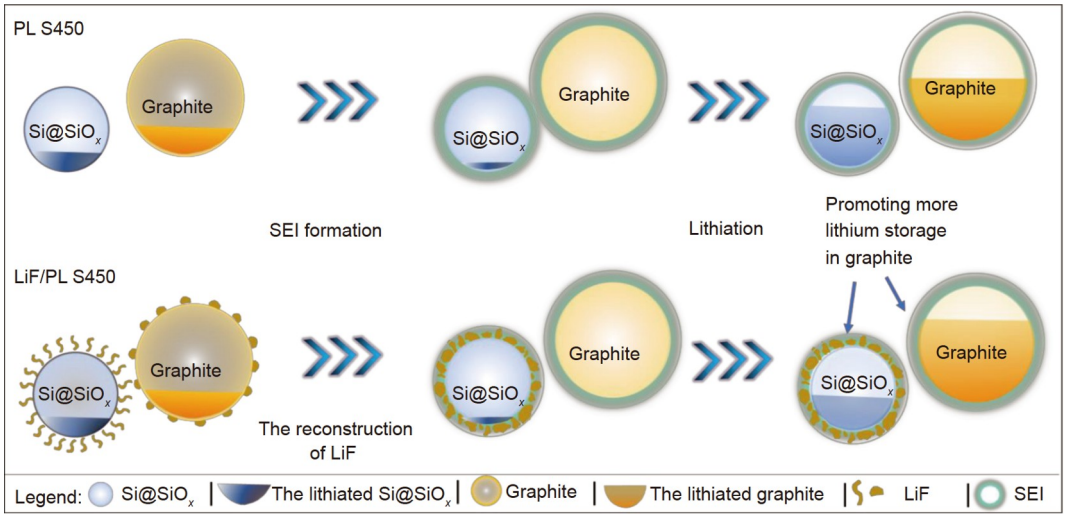

Scheme 1 Schematic illustration of SEI formation and the lithiation states of different anodes. From left-to-right: the original state of the anodes; the state of the anodes after they are immersed in the electrolyte; and the lithiated state of the anodes. The yellow and blue circles represent the state of graphite and Si@SiO_x in different anodes, respectively.

with a 3.2-mm probe. The sample rotation rate was 12 kHz. The ^{7}Li chemical shift was referenced to solid ^{7}LiCl and trimethylsilylpropanoic acid (both at 0 ppm). The ^{6}Li chemical shift was referenced to solid ^{6}LiCl and trimethylsilylpropanoic acid (both at 0 ppm). Electron energy loss spectroscopy (EELS) patterns were recorded on an FEI Tecnai F20 transmission electron microscope. Scanning TEM was performed using a JEOL 2100F (Tokyo, Japan) transmission electron microscope operated at 200 kV. Samples were prepared in an Ar-filled glove box. To quantify the residual lithium species in the S450 anode, the sample was placed in a titration vessel with a septum port and attached to an in-line mass spectrometer (MS), while an air-free environment was maintained in the vessel. After the vessel was attached and a baseline MS was acquired, 1 mL D_2O was injected into the vessel, leading to D_2 evolution.

Theoretical calculations

First-principles density functional theory (DFT) calculations were performed to study the graphite-, SiO-, Li_2O-, Li_2CO_3-, $Li_{15}Si_4$-, and Li_4SiO_4-LiF interfaces using the Vienna *Ab Initio* Simulation Package and applying a Projector Augmented Wave method. The exchange-correlation energy was described by the Perdew, Burke, and Ernzerhof functional. The energy cutoff for the electron wavefunction was set to 520 eV. Geometry optimizations were performed using the conjugated gradient method, and the convergence thresholds were set to 10^{-5} eV (energy) and 0.02 eV Å^{-1} (force). The work of separation (W_{sep}) for the graphite-, SiO-, Li_2O-, Li_2CO_3-, $Li_{15}Si_4$-, and Li_4SiO_4-LiF interfaces were defined by Equation (1),

$$W_{sep} = (E_x + E_{LiF} - E_{x\text{-}LiF}) / A, \quad (1)$$

where E_x, E_{LiF}, and $E_{x\text{-}LiF}$ represent the total energy of the x (where x = C, SiO, Li_2O, Li_2CO_3, $Li_{15}Si_4$, or Li_4SiO_4) slab, LiF slab, and x-LiF interface, respectively, and A represents the total interfacial area. To model the slabs, a vacuum layer larger than 15 Å was applied for the x-LiF interface.

RESULTS AND DISCUSSION

Selective LiF-induced lithiation strategy based on the work of separation calculations

The high modulus, poor electrical conductivity, and wide band gap of a LiF-rich SEI are beneficial in terms of promoting the cyclability of silicon-based batteries [42]. DFT calculations indicate that the ideal work of separation (W_{sep}) can be used to model the energy required for the idealized separation of the interface into two surfaces in a vacuum. The more positive the value of W_{sep}, the easier it is to form a new surface [42]; however, the W_{sep} between LiF and various materials in the silicon-system varies widely. The LiF-Li_4SiO_4 interface and the LiF-$Li_{15}Si_4$ interface correspond to the highest W_{sep} values, and the W_{sep} of the LiF/graphite interface is negative, meaning that LiF tends to bind with the surface of Si@SiO_x. When LiF is deposited on an anode composite, the selective distribution of LiF can be predicted based on this W_{sep} difference.

To visualize this relationship, nanostructured LiF was introduced to the composite anode *via* magnetron sputtering. The SEM images show that LiF appeared as whiskers on the Si@SiO_x and as papules on the graphite after magnetron sputtering (Fig. 1b, Figs S1 and S2a–c). This difference in morphology is likely caused by distinct W_{sep} values or degrees of lattice matching [44]. Interestingly, the whiskers and papules disappeared after the anodes were immersed in the electrolyte because of the relatively high solubility of LiF compared with other components at the SEI. Meanwhile, a LiF self-assembly process (i.e., dissolution-redeposition) occurred with the formation of the SEI. Consistent with the computational results, the redistribution of LiF was observed as the LiF was preferentially deposited on the Si@SiO_x surface (Fig. 1b, c and Fig. S2d–g). It is also clear from the TEM images that LiF was uniformly distributed on the surface of Si@SiO_x (Fig. 1d, e). EELS suggested that the LiF mixed with lithium silicate and other components appeared on the Si@SiO_x surface (Fig. 1f–i and Fig. S3) [45,46]. The differences in W_{sep} between LiF and the active materials confirmed the successful targeted regulation of Si@SiO_x by LiF.

Because LiF exhibits poor electronic and ionic conductivity, the LiF-rich SEI on the surface of Si@SiO_x should increase the interfacial lithium-ion and electron transport resistance at the Si@SiO_x interface. Thus, the lithiation potential of LiC_x and $Li_{15}Si_4$ in the pre-lithiated anode can be distinguished. Meanwhile, the LiF serves as a "lithium distributor" to promote active lithium stores in the graphite, which exhibits higher conductivity than Si@SiO_x. This behavior is critical for improving cyclability by unshackling the highly reversible lithium storage capabilities from the redundant capacity of the anode.

In a full cell, the redundant capacity is necessary to ensure the storage of lithium ions from the cathode and to prevent lithium metal plating. In this work, the N/P ratio is 1.09, which means that nearly 10% of the pre-lithiated anode capacity is redundant (without pre-lithiation, the redundant capacity is greater than 10%). When the anode is lithiated, $Li_{15}Si_4$ forms simultaneously with graphite lithiation because of their similar lithiation potentials; both silicon and graphite contribute to the redundancy capacity (Scheme 1). This distribution is unfavorable because the graphite with highly reversible lithium storage capability is underused, while the $Li_{15}Si_4$ causes severe volume deformation. This phenomenon is more pronounced in a pre-lithiated anode. Because of the lower lithiation potential of the pre-lithiated anode, more $Li_{15}Si_4$ is formed, even if the graphite has a substantial redundancy capacity.

Through sufficient potential separation, LiF can serve as a "lithium distributor" to unshackle the highly reversible lithium storage capacity (i.e., the redundancy capacity) of graphite in a pre-lithiated anode-based full cell, while limiting the formation of $Li_{15}Si_4$ (Scheme 1). Thus, it is reasonable to expect enhanced cycling stability for a pre-lithiated high-loading composite anode.

Characterization of pre-lithiated anodes with/without regulation

As shown in Fig. S4, the initial discharge specific capacity of the as-assembled NCA/S450 cell without pre-lithiation is approximately 170 mA h g^{-1} (based on the weight of NCA) over the potential range of 2.8–4.2 V, which is below the capacity obtained in the half-cell (NCA/Li, 190 mA h g^{-1}, Fig. S5). The relevant calculations suggest that 3.3 μm of deposited lithium is needed to compensate for the 20 mA h g^{-1} capacity loss (the calculations are detailed in the Supplementary information). Therefore, we began our investigations using the S450 anode, which was pre-loaded with 3.3 μm lithium and labeled as PL S450. The discharge curve of PL S450 shows that the discharge capacity increased to 190 mA h g^{-1} and the ICE increased to 84% following the compensation for the active lithium loss (Fig. S4). Notably, the voltage-capacity curves in Fig. S4e show

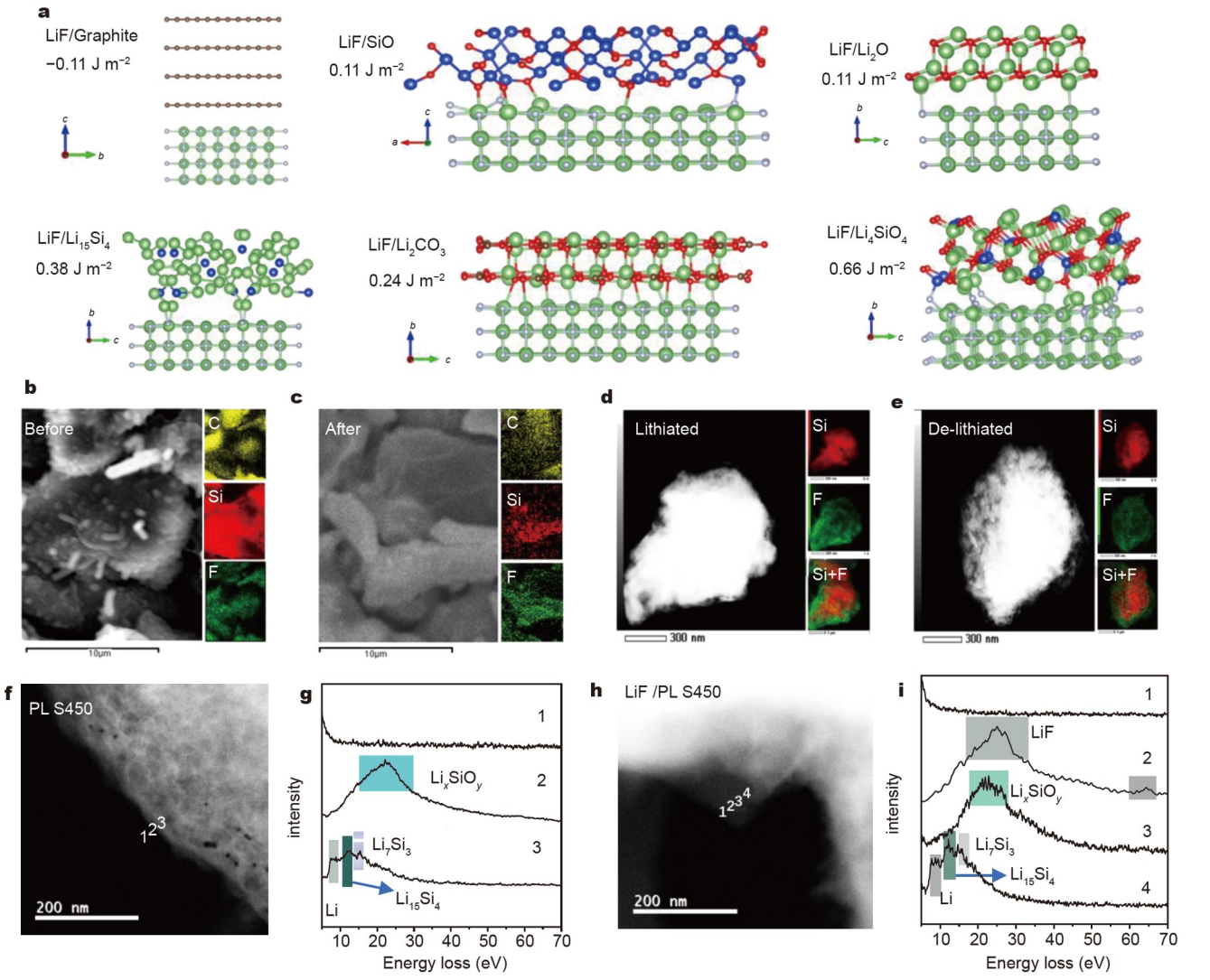

Figure 1 (a) The calculated W_{sep} results for different interfaces. Representative SEM images and the corresponding elemental maps of the LiF/PL S450 anode (b) before and (c) after it was immersed in the electrolyte. Typical TEM images and the corresponding elemental maps of the LiF/PL S450 anode in the (d) lithiated and (e) delithiated states. High-angle annular dark-field images and the corresponding EELS spectra (labeled 1–4 from the surface to the inner layers) captured near the surface of the Si@SiO_x particles in (f, g) lithiated PL S450 and (h, i) lithiated LiF/PL S450. The characteristic peak positions for various species are indicated by color blocks in the EELS spectra.

that the pre-lithiated anode with added LiF (LiF/PL S450) exhibited increased polarization compared with PL S450 because of the insulating nature of LiF.

To monitor the evolution of the active lithium in the S450, PL S450, and LiF/PL S450 samples, we performed solid state NMR (SSNMR) characterizations. In these experiments, ^{6}Li was integrated to trace the pre-loaded lithium in the PL S450 (Fig. 2a). With the exception of the samples in Fig. 2a, the remaining pre-lithiated samples were pre-lithiated with ^{7}Li (Fig. 2b–d) to facilitate further analysis. Fig. 2a displays the ^{6}Li NMR spectra of the as-prepared PL S450 and the PL S450 after immersion in liquid electrolyte. The main peaks in the former spectrum include signals from Li_xSi (where $x < 2.0$) and LiC_x, whereas the latter spectrum only includes peaks attributed to lithium salts (near 0 ppm) and $Li_{12}Si_7$ (17 ppm). The lithium salts originated from the SEI formation, which consumed the pre-loaded lithium. When the full cell is charged to 4.2 V, the anode is lithiated, and the PL S450 anode displays Li signals at 45, 12, and −5 ppm, corresponding to LiC_x, Li_xSi ($2.0 < x < 3.5$), and $Li_{15}Si_4$, respectively (Fig. 2c) [3,47].

Compared with the lithiated S450 anode (Fig. 2b), the relative integrated peak areas of the LiC_x and $Li_{15}Si_4$ signals notably increased in the lithiated PL S450 anode because of the greater degree of lithiation. Because LiC_x and $Li_{15}Si_4$ have similar formation potentials (70–100 mV), $Li_{15}Si_4$ inevitably increases as LiC_x increases. The increased proportion of $Li_{15}Si_4$ is a serious concern for the pre-lithiated anode. The volume deformation related to $Li_{15}Si_4$ formation can cause the fracture and regeneration of the SEI, as well as electrical contact failures. Moreover, it aggravates the loss of the active lithium in the anode, thereby influencing the cycling performance. The NMR results reveal a LiC_x peak in the lithiated LiF/PL S450 anode spectrum whose integrated area increased compared with that in the PL S450 spectrum. More importantly, the integrated peak area corresponding to $Li_{15}Si_4$ decreased (Fig. 2d). Therefore, by exploiting the W_{sep} difference to separate the potentials of LiC_x and $Li_{15}Si_4$, we effectively unshackled the highly reversible lithium storage capabilities from the redundant capacity in the anode; moreover,

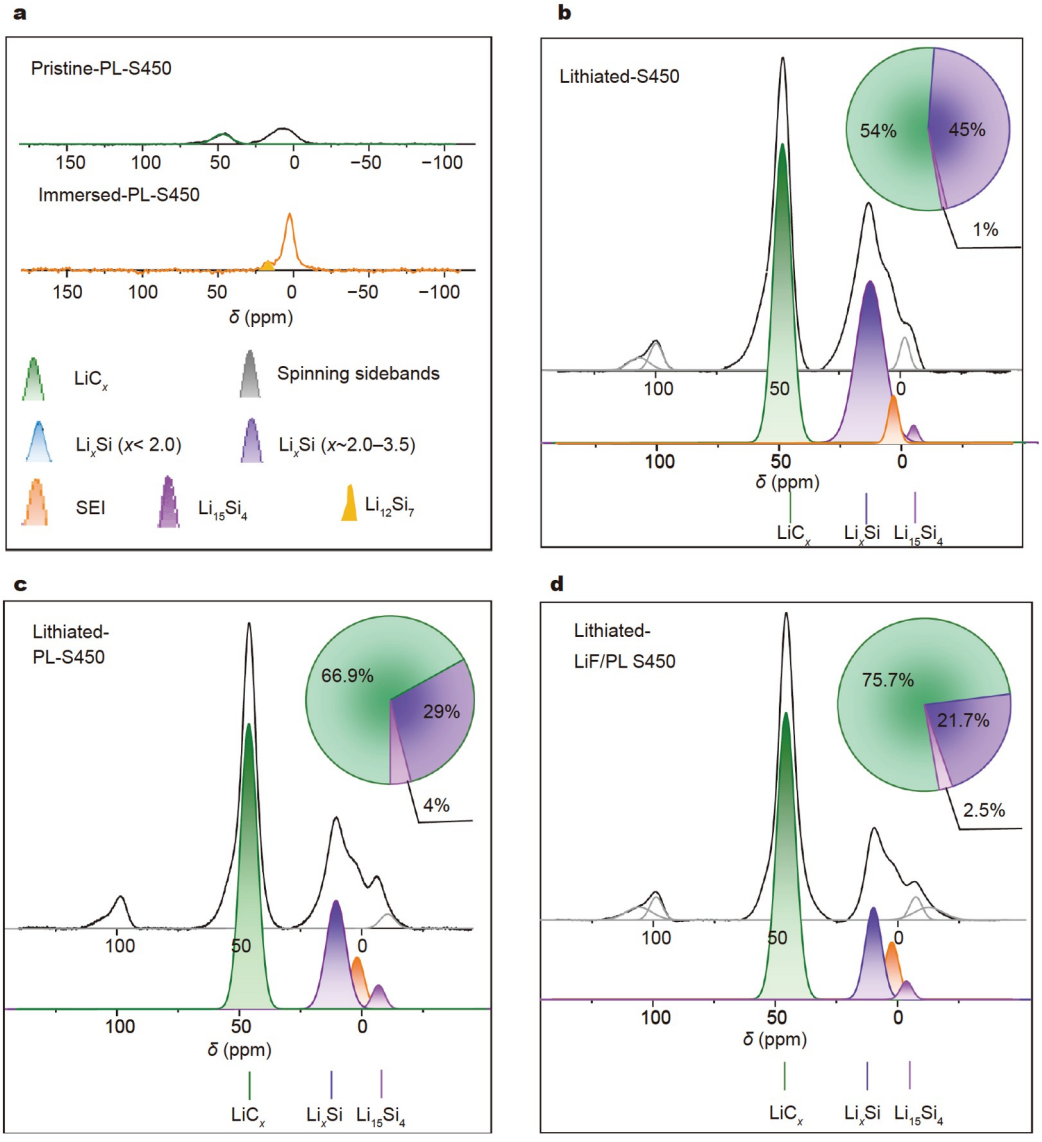

Figure 2 Original Li magic angle spinning (MAS) NMR single-pulse excitation spectra (black lines) and the spectra after processing (colored). (a) Pristine PL S450 and PL S450 anodes after being immersed in liquid electrolyte (^{6}Li). (b) Lithiated S450 and the integrated peak area proportions of LiC_x, Li_xSi, and $Li_{15}Si_4$ (^{7}Li). (c) Lithiated PL S450 and the integrated peak area proportions of LiC_x, Li_xSi, and $Li_{15}Si_4$ (^{7}Li). (d) Lithiated LiF/PL S450 and the integrated peak area proportions of LiC_x, Li_xSi, and $Li_{15}Si_4$ (^{7}Li).

this significantly mitigated the active lithium loss caused by Si@SiO_x-derived species.

To experimentally confirm the analysis described above, the anode was disassembled from the full cell after a lithiation/delithiation cycle and reassembled into a half-cell (with new lithium metal as the anode). The half-cell was then charged to 1.5 V to complete the delithiation process (Fig. 3a). Because the lithium storage species can react with H_2O to produce H_2, we performed a D_2O titration to determine the extent of lithium storage available in the irreversible species that remained at the delithiated anodes (detailed experimental methods are provided in the Supplementary information, Scheme S2 and Fig. S6) [48]. These species are mainly generated because of the loss of electric contact due to the volume deformation (which can be partially recovered by applying additional pressure to the anode; Fig. S7), rather than SEI components resulting from a parasitic reaction. The histogram describing the D_2O titrations (Fig. 3b) indicates that the amount of "irreversible lithium" in the PL S450 is much higher than that in the non-pre-lithiated S450; moreover, there is a remarkable increase from the 1st cycle to the 60th cycle. These results confirm that the increased proportion of $Li_{15}Si_4$ in the anode generates more irreversible lithium because of severe volume deformation. The volume deformation also causes the rupture and reconstruction of the SEI on Si@SiO_x, which accelerates the parasitic reaction. Consistent with the NMR results, there is markedly less "irreversible lithium" in the LiF/PL S450 anode than in the PL S450 anode. This observation verifies that the side reactions and active lithium loss related to electrical contact failure can be reduced by unshackling the reversible capacity.

Cell performance as a function of the amount of pre-loaded lithium

Consistent with the analysis described above, the LiF/PL (3.3) S450 anode exhibits better cycling stability than the PL (3.3) S450 anode (both have 3.3 μm of pre-loaded lithium) and the

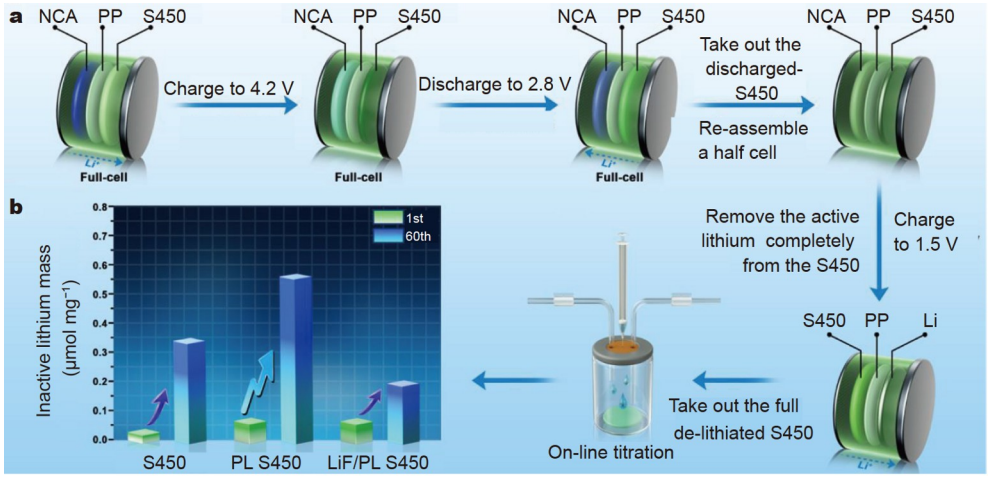

Figure 3 (a) Schematic illustration of the sample preparation process for titration experiments. The color of the NCA and S450 materials ranges from dark to light, indicating that the lithium contents range from high to low, respectively. (b) Comparison of the inactive lithium masses in the S450, PL S450, and LiF/PL S450 anodes.

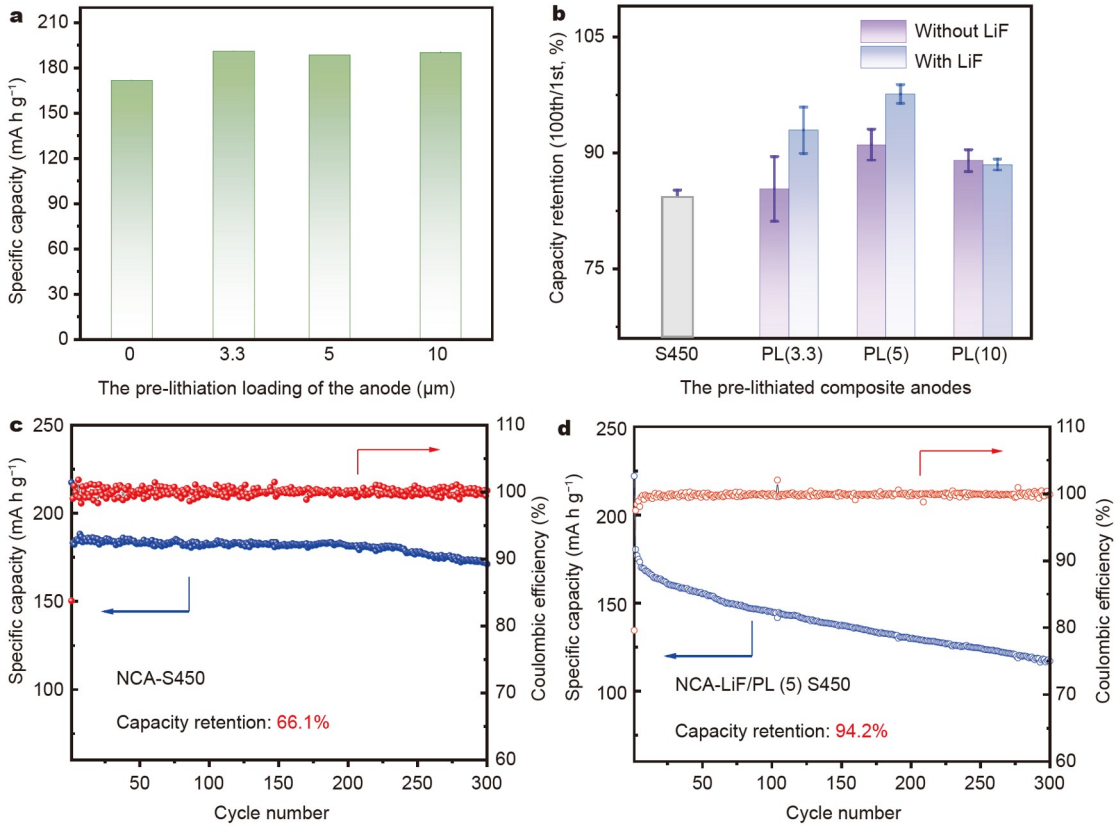

Figure 4 (a) Initial specific capacities of the full cells (NCA-S450), where different amounts of lithium were pre-loaded onto the S450. (b) Capacity retention ($100^{th}/1^{st}$) of the full cells (NCA-S450), where different amounts of lithium were pre-loaded onto the S450; the comparison includes anodes with and without added LiF. Cycling performances and ICE of (c) the NCA-S450 and (d) NCA-LiF/PL (5) S450 (rate = 0.2 C/0.4 C). The NCA and S450 anodes in these experiments had an active mass loading of ~26 and 12.1 mg cm^{-2}, respectively.

S450 anode (Fig. 4b, c and Fig. S8), with a full cell capacity retention of 88% over 200 cycles. Considering these relationships, we further increased the amount of pre-loaded lithium to 5 μm (and labeled the sample PL (5) S450) to more effectively harness the highly reversible lithiation capability of the graphite in the anode. In this case, more of the active lithium will be stored in the form of LiC_x (and $Li_{15}Si_4$ when the anode is charged), which means that more severe volume deformation and side reactions will occur upon cycling. As a result of regulation, the active lithium that exceeds the cathode's capacity can be appropriately stored in the form of LiC_x when the anode is charging, thereby further unshackling the highly reversible lithium storage capabilities from the redundant capacity; this can effectively compensate for the inevitable but minimized active lithium loss during cycling. As expected, the battery (i.e., LiF/PL (5) S450) exhibited enhanced cycling stability, with a capacity

retention of 94.2% over 300 cycles and an ICE of 84% (Fig. 4d and Fig. S4c). Therefore, we combined the commercial S450 anode (5.4 mA h cm^{-2}) with a high-loading cathode (4.9 mA h cm^{-2}), both of which were considered ultra-high loading in the context of industrial applications. Based on the mass of the cell, the NCA-PL (5) S450 had an estimated gravimetric energy density of 309 W h kg^{-1} in a 50 A h pouch cell (Table S1). In general, lithium deposition should be avoided, even when LiF is introduced. As shown in Fig. 4b, when the quantity of pre-loaded lithium exceeds the capacity of the S450 anode material (in the present case, 10 μm lithium was deposited at the anode), lithium deposition occurs during the charging process. Although the cell can deliver an ICE of 84% with a 190 mA h g^{-1} discharge capacity (Fig. 4a), the capacity decays sharply (Fig. 4b, Figs S9 and S10). This result indicates that the LiF can no longer effectively prevent severe active lithium loss caused by the direct deposition of lithium metal on the anode.

CONCLUSIONS

In summary, a selective LiF-induced lithiation strategy based on W_{sep} calculations was proposed and successfully implemented to unshackle the highly reversible capacity from the redundancy capacity of silicon-based composite anodes, thereby improving their cycling stabilities. The LiF preferentially redeposits on the Si@SiO_x surface following a well-designed route, which enables differentiation (i.e., separation) of the lithiation potentials of LiC_x and $Li_{15}Si_4$ to facilitate selective lithiation in the composite system. This approach allows for complete use of the graphite that originally accounted for most of the redundancy capacity. Meanwhile, $Li_{15}Si_4$ formation is reduced, and the volume deformation is dramatically alleviated. Reasonably increasing the amount of pre-loaded lithium, which provides a stable lithium source to compensate for active lithium loss during cycling, promotes better cycling stability. This study experimentally demonstrated that a capacity retention of 94.2% over 300 cycles can be achieved in a LiF-PL S450/NCA full cell with a high area capacity (4.9 mA h cm^{-2}). The novel strategy presented herein is particularly feasible for practical industrial applications because it requires no changes to the existing (mature) manufacturing process. Overall, the strategy developed based on exploiting differences in interface separation energy provides an unprecedented approach for regulating composite systems.

Received 22 December 2021; accepted 23 March 2022; published online 8 June 2022

1 Tian H, Tian H, Yang W, *et al.* Stable hollow-structured silicon suboxide-based anodes toward high-performance lithium-ion batteries. Adv Funct Mater, 2021, 31: 2101796
2 Reynier Y, Vincens C, Leys C, *et al.* Practical implementation of Li doped SiO in high energy density 21700 cell. J Power Sources, 2020, 450: 227699
3 Kitada K, Pecher O, Magusin PCMM, *et al.* Unraveling the reaction mechanisms of SiO anodes for Li-ion batteries by combining *in situ* ^{7}Li and *ex situ* ^{7}Li/^{29}Si solid-state NMR spectroscopy. J Am Chem Soc, 2019, 141: 7014–7027
4 Berhaut CL, Dominguez DZ, Tomasi D, *et al.* Prelithiation of silicon/graphite composite anodes: Benefits and mechanisms for long-lasting Li-ion batteries. Energy Storage Mater, 2020, 29: 190–197
5 Bärmann P, Mohrhardt M, Frerichs JE, *et al.* Mechanistic insights into the pre-lithiation of silicon/graphite negative electrodes in "dry state" and after electrolyte addition using passivated lithium metal powder. Adv Energy Mater, 2021, 11: 2100925
6 Holtstiege F, Wilken A, Winter M, *et al.* Running out of lithium? A route to differentiate between capacity losses and active lithium losses in lithium-ion batteries. Phys Chem Chem Phys, 2017, 19: 25905–25918
7 Suh SS, Yoon WY, Kim DH, *et al.* Electrochemical behavior of SiO_x anodes with variation of oxygen ratio for Li-ion batteries. Electrochim Acta, 2014, 148: 111–117
8 Zhao J, Lee HW, Sun J, *et al.* Metallurgically lithiated SiO_x anode with high capacity and ambient air compatibility. Proc Natl Acad Sci USA, 2016, 113: 7408–7413
9 Stetson C, Schnabel M, Li Z, *et al.* Microscopic observation of solid electrolyte interphase bilayer inversion on silicon oxide. ACS Energy Lett, 2020, 5: 3657–3662
10 Liu XH, Wang JW, Huang S, *et al. In situ* atomic-scale imaging of electrochemical lithiation in silicon. Nat Nanotech, 2012, 7: 749–756
11 Goriparti S, Miele E, De Angelis F, *et al.* Review on recent progress of nanostructured anode materials for Li-ion batteries. J Power Sources, 2014, 257: 421–443
12 Magasinski A, Dixon P, Hertzberg B, *et al.* Erratum: High-performance lithium-ion anodes using a hierarchical bottom-up approach. Nat Mater, 2010, 9: 461
13 Meschini I, Nobili F, Mancini M, *et al.* High-performance Sn@carbon nanocomposite anode for lithium batteries. J Power Sources, 2013, 226: 241–248
14 Usui H, Nouno K, Takemoto Y, *et al.* Influence of mechanical grinding on lithium insertion and extraction properties of iron silicide/silicon composites. J Power Sources, 2014, 268: 848–852
15 Li T, Cao YL, Ai XP, *et al.* Cycleable graphite/$FeSi_6$ alloy composite as a high capacity anode material for Li-ion batteries. J Power Sources, 2008, 184: 473–476
16 Hwa Y, Park CM, Sohn HJ. Modified SiO as a high performance anode for Li-ion batteries. J Power Sources, 2013, 222: 129–134
17 Park K, Yu BC, Goodenough JB. Li_3N as a cathode additive for high-energy-density lithium-ion batteries. Adv Energy Mater, 2016, 6: 1502534
18 Bie Y, Yang J, Wang J, *et al.* Li_2O_2 as a cathode additive for the initial anode irreversibility compensation in lithium-ion batteries. Chem Commun, 2017, 53: 8324–8327
19 Zhan Y, Yu H, Ben L, *et al.* Using Li_2S to compensate for the loss of active lithium in Li-ion batteries. Electrochim Acta, 2017, 255: 212–219
20 Du J, Wang W, Sheng Eng AY, *et al.* Metal/LiF/Li_2O nanocomposite for battery cathode prelithiation: Trade-off between capacity and stability. Nano Lett, 2020, 20: 546–552
21 Kim KH, Shon J, Jeong H, *et al.* Improving the cyclability of silicon anodes for lithium-ion batteries using a simple pre-lithiation method. J Power Sources, 2020, 459: 228066
22 Jin L, Shen C, Wu Q, *et al.* Pre-lithiation strategies for next-generation practical lithium-ion batteries. Adv Sci, 2021, 8: 2005031
23 Watanabe T, Tsuda T, Ando N, *et al.* An improved pre-lithiation of graphite anodes using through-holed cathode and anode electrodes in a laminated lithium ion battery. Electrochim Acta, 2019, 324: 134848
24 Lee JI, Park S. High-performance porous silicon monoxide anodes synthesized *via* metal-assisted chemical etching. Nano Energy, 2013, 2: 146–152
25 Meng Q, Li G, Yue J, *et al.* High-performance lithiated SiO_x anode obtained by a controllable and efficient prelithiation strategy. ACS Appl Mater Interfaces, 2019, 11: 32062–32068
26 Li X, Gu M, Hu S, *et al.* Mesoporous silicon sponge as an anti-pulverization structure for high-performance lithium-ion battery anodes. Nat Commun, 2014, 5: 4105
27 Wang GX, Ahn JH, Yao J, *et al.* Nanostructured Si-C composite anodes for lithium-ion batteries. Electrochem Commun, 2004, 6: 689–692
28 Hwa Y, Kim WS, Hong SH, *et al.* High capacity and rate capability of core-shell structured nano-Si/C anode for Li-ion batteries. Electrochim Acta, 2012, 71: 201–205
29 Zhang M, Hou X, Wang J, *et al.* Interweaved Si@C/CNTs&CNFs composites as anode materials for Li-ion batteries. J Alloys Compd, 2014, 588: 206–211
30 Chen Y, Hu Y, Shao J, *et al.* Pyrolytic carbon-coated silicon/carbon nanofiber composite anodes for high-performance lithium-ion bat-

teries. J Power Sources, 2015, 298: 130–137
31 Xu Q, Li JY, Sun JK, *et al.* Watermelon-inspired Si/C microspheres with hierarchical buffer structures for densely compacted lithium-ion battery anodes. Adv Energy Mater, 2017, 7: 1601481
32 Chen W, Salvatierra RV, Ren M, *et al.* Laser-induced silicon oxide for anode-free lithium metal batteries. Adv Mater, 2020, 32: 2002850
33 Deng K, Han D, Ren S, *et al.* Single-ion conducting artificial solid electrolyte interphase layers for dendrite-free and highly stable lithium metal anodes. J Mater Chem A, 2019, 7: 13113–13119
34 Fedorov RG, Maletti S, Heubner C, *et al.* Molecular engineering approaches to fabricate artificial solid-electrolyte interphases on anodes for Li-ion batteries: A critical review. Adv Energy Mater, 2021, 11: 2101173
35 Reyes Jiménez A, Nölle R, Wagner R, *et al.* A step towards understanding the beneficial influence of a LIPON-based artificial SEI on silicon thin film anodes in lithium-ion batteries. Nanoscale, 2018, 10: 2128–2137
36 Subramanya U, Chua C, He Leong VG, *et al.* Carbon-based artificial SEI layers for aqueous lithium-ion battery anodes. RSC Adv, 2020, 10: 674–681
37 Tu Z, Zachman MJ, Choudhury S, *et al.* Stabilizing protic and aprotic liquid electrolytes at high-bandgap oxide interphases. Chem Mater, 2018, 30: 5655–5662
38 Zhao J, Lu Z, Wang H, *et al.* Artificial solid electrolyte interphase-protected Li_xSi nanoparticles: An efficient and stable prelithiation reagent for lithium-ion batteries. J Am Chem Soc, 2015, 137: 8372–8375
39 Ogata K, Salager E, Kerr CJ, *et al.* Revealing lithium-silicide phase transformations in nano-structured silicon-based lithium ion batteries *via in situ* NMR spectroscopy. Nat Commun, 2014, 5: 3217
40 Xia M, Li Y, Wu Y, *et al.* Improving the electrochemical properties of a SiO@C/graphite composite anode for high-energy lithium-ion batteries by adding lithium fluoride. Appl Surf Sci, 2019, 480: 410–418
41 Chen Z, Zhang L, Wu X, *et al.* Effect of N/P ratios on the performance of $LiNi_{0.8}Co_{0.15}Al_{0.05}O_2$||SiO/graphite lithium-ion batteries. J Power Sources, 2019, 439: 227056
42 Lepley ND, Holzwarth NAW. Modeling interfaces between solids: Application to Li battery materials. Phys Rev B, 2015, 92: 214201
43 Markevich E, Salitra G, Chesneau F, *et al.* Very stable lithium metal stripping-plating at a high rate and high areal capacity in fluoroethylene carbonate-based organic electrolyte solution. ACS Energy Lett, 2017, 2: 1321–1326
44 Sugawara A, Mae K. Surface morphology of epitaxial LiF(110) and CaF_2 (110) layers. J Vac Sci Technol B, 2005, 23: 443
45 Boniface M, Quazuguel L, Danet J, *et al.* Nanoscale chemical evolution of silicon negative electrodes characterized by low-loss STEM-EELS. Nano Lett, 2016, 16: 7381–7388
46 Chen J, Fan X, Li Q, *et al.* Electrolyte design for LiF-rich solid-electrolyte interfaces to enable high-performance microsized alloy anodes for batteries. Nat Energy, 2020, 5: 386–397
47 Holtstiege F, Schmuch R, Winter M, *et al.* New insights into prelithiation kinetics of graphite anodes *via* nuclear magnetic resonance spectroscopy. J Power Sources, 2018, 378: 522–526
48 Xu G, Li J, Wang C, *et al.* The formation/decomposition equilibrium of LiH and its contribution on anode failure in practical lithium metal batteries. Angew Chem Int Ed, 2021, 60: 7770–7776

Acknowledgements This work was supported by the Key-Area Research and Development Program of Guangdong Province (2020B090919005), the National Key R&D Program of China (2017YFE0127600), the Strategic Priority Research Program of the Chinese Academy of Sciences (XDA22010600), Taishan Scholars Program for Young Expert of Shandong Province (tsqn 202103145), the National Natural Science Foundation of China (22179135), and the Finance Science and Technology Project of Hainan province (ZDKJ202014). We also acknowledge the assistance of Prof. Lin Gu and Dr. Qinghua Zhang from Beijing National Laboratory for Condensed Matter Physics, Institute of Physics, Chinese Academy of Sciences for Low-loss STEM-EELS testing.

Author contributions Sun J, Dong S and Cui G conceived the idea for the project. Zhang S conducted the DFT calculations. Sun J, Xin Y, Liu H, Li J, Liu T, and Wang C prepared the materials and performed the electrochemical experiments. Gu L and Zhang Q conducted the EELS spectra. Cui G, Dong S, Ma J, Sun J and Lu C analyzed the data and drafted the manuscript.

Conflict of interest The authors declare that they have no conflict of interest.

Supplementary information Experimental details and supporting data are available in the online version of the paper.

Jinran Sun received her bachelor's degree in 2018. Now she is a PhD candidate in Prof. Guanglei Cui's group at Qingdao Institute of Bioenergy and Bioprocess Technology (QIBEBT), Chinese Academy of Sciences. Her current research is the design and optimization of high specific energy density lithium battery.

Shu Zhang obtained the PhD degree of condensed matter physics from the University of Chinese Academy of Sciences in 2015. Now she is an assistant professor at QIBEBT, Chinese Academy of Sciences. Her research centers on the solid-state lithium batteries and the applications of theoretical simulation for chemistry and materials science.

Shamu Dong is currently a professor of QIBEBT. He obtained his PhD degree from QIBEBT, Chinese Academy of Sciences in 2012. Then he joined the institute and continued his research on highly efficient energy-storage materials. His current research focuses on the electrolyte system of metal batteries.

Guanglei Cui is currently a professor and the leader of the Solid Energy System Technology Center, the director of the Applied Energy Technology Division, and the deputy director of the Academic Committee of QIBEBT. His research topics include sustainable and highly efficient energy storage materials, all-solid-state batteries and novel energy devices.

LiF引发选择性锂化提升硅碳负极可逆容量

孙金燃[1,2†], 张舒[1†], 张庆华[3], 辛云川[1], 董杉木[1*], 刘海胜[1], 李杰东[1], 王超[1], 鲁承龙[1], 杨武海[1], 刘亭亭[1,2], 马君[1], 谷林[3], 崔光磊[1,2*]

摘要 Si@SiO_x/C复合负极具有较高比容量, 被认为是锂离子电池实际工业应用中最有前途的负极材料. 然而, 由于硅的严重体积形变, 复合负极的循环稳定性依然面临巨大挑战. 本工作通过释放负极冗余容量中高度可逆的锂储存能力, 提高了复合负极的循环稳定性. 基于LiF与不同活性材料之间的界面分离能差, 我们针对复合负极提出了一种LiF引发的选择性锂化策略. LiF在Si@SiO_x上发生再沉积并富集, 分离LiC_x和$Li_{15}Si_4$的形成电位, 进而促进锂离子在石墨中的存储(未修饰前复合负极中石墨的容量未被充分利用). 因此, 在不牺牲比容量的前提下, 全电池获得了更好的倍率性能和循环性能. 超高面容量(NCA/S450, 4.9 mA h cm^{-2})的全电池经300次循环后, 容量保持率从66.1%显著提高到94.2%. 选择性锂化策略在实际工业应用中更加可行, 不需要改变现有的电池制造工艺. 本研究为长循环寿命硅/石墨复合负极的开发开辟了新途径.

